A Comparison of the Impact of Two Time-differencing Schemes on the NASA–GLAS Climate Model*

RICHARD L. PFEFFER

Geophysical Fluid Dynamics Institute and Department of Meteorology, Florida State University, Tallahassee, Florida

I. M. NAVON

*Department of Mathematics, Supercomputer Computations Research Institute and Geophysical
Fluid Dynamics Institute, Florida State University, Tallahassee, Florida*

XIAOLEI ZOU

Supercomputer Computations Research Institute, Florida State University, Tallahassee, Florida

(Manuscript received 27 February 1991, in final form 25 October 1991)

ABSTRACT

This paper presents evidence of the sensitivity of a general circulation model (GCM) to the time-differencing scheme employed when the physical parameterizations and space discretization are not changed. For this purpose, two time-marching schemes—the leapfrog and the Matsuno schemes—are analyzed and tested on the National Aeronautics and Space Administration–Goddard Laboratory for Atmospheric Studies (NASA–GLAS) fourth-order GCM in terms of the stability and behavior of 2-month–averaged fields. Linear analysis suggests that Rossby waves are slightly damped and slightly accelerated when the Matsuno scheme is used and that these effects are scale selective, being smallest for the longest waves. It also suggests that such waves are accelerated less and are not damped when the leapfrog scheme is used. An empirical orthogonal function analysis of the meridional component of velocity at 46°N, keeping at least 70% of the variance, reveals less shortwave activity in the numerical solution with the Matsuno scheme but does not lend support to the conclusion that the waves are accelerated less in the solution with the leapfrog scheme.

The two-dimensional Eliassen–Palm (E–P) flux divergence and the eddy-induced mean meridional circulation are found to be stronger in the simulation with the leapfrog time-differencing scheme than in the one with the Matsuno scheme, suggesting that the transient-wave activity is damped by the Matsuno scheme. On the other hand, the three-dimensional stationary-wave activity flux in the Northern Hemisphere simulated with the Matsuno scheme is more intense than that simulated with the leapfrog scheme, indicating that the stationary waves are more robust in the integration with the Matsuno scheme.

The GCM precipitation when integrated with the leapfrog scheme is much more intense over the tropical western Pacific and the northeastern Pacific and less intense over the western North Atlantic Ocean. The kinetic energy of waves with wavenumber greater than 9 simulated by the Matsuno scheme is consistently smaller than that obtained by the leapfrog scheme. These results give evidence that climate simulations are sensitive not only to physical parameterizations of subgrid-scale processes but also to the numerical methodology employed.

1. Introduction

General circulation models (GCMs) are the most elaborate of a hierarchy of mathematical models used in the study of climate. A general review of atmospheric GCMs presented by Simmons and Bengtsson (1984) emphasizes the importance of physical processes in determining the behavior of climatic systems. GCMs have

been used for seasonal simulation (Shukla et al. 1981) as well as for studying climate variability on time scales of a month and upward. In particular, studies have been conducted to determine the sensitivity of atmospheric GCMs to changes in physical mechanisms such as surface albedo (Charney 1975), sea-ice limits in the Arctic (Herman and Johnson 1978), low-frequency variability (Charney and Shukla 1981), and inadequate orographic effects (Wallace et al. 1983).

Reviews of the numerical techniques used in numerical weather prediction models and GCMs have been presented by Mesinger and Arakawa (1976) and Kasahara (1979). Numerical experiments in which the earth's climate is simulated using different numerical schemes can play a valuable role in clarifying the nature

---

* Contribution No. 328 of the Geophysical Fluid Dynamics Institute

---

Corresponding author address: Professor Richard L. Pfeffer, Geophysical Fluid Dynamics Institute, Florida State University, Tallahassee, FL 32306.

of individual GCMs. This in turn may help in the design of more comprehensive models and aid in the interpretation of results. A comparison of spectral and finite-difference simulations of climate circulations was carried out by Gutowski et al. (1990). Their results showed that the spectral and gridpoint methods do not produce identical model climatology. In this paper we examine the effect of two different time-differencing schemes, namely the Matsuno (Euler-backward) and the leapfrog scheme, for a seasonal climate integration of the National Aeronautics and Space Administration–Goddard Laboratory for Atmospheric Studies (NASA–GLAS) fourth-order general circulation model.

The integration presented here uses seasonal varying solar forcing and boundary conditions of sea surface temperature (SST), soil moisture, sea-ice extent, snow, and surface albedo. Section 2 presents a brief description of the model equations. Section 3 describes the two time-differencing schemes and presents a brief survey of their numerical stability analysis. Comparison of the model results using the two time-differencing schemes to simulate the climate during January and February are presented in section 4 for the Eliassen–Palm (E–P) flux, the eddy-induced meridional circulation, the three-dimensional wave activity flux, the leading empirical orthogonal functions (EOFs), the precipitation, and the kinetic energy spectrum. Section 5 gives a summary and discussion.

2. Model description

The model used for this study was the NASA–GLAS GCM, which has been described in detail by Kalnay et al. (1983). The model equations, expressed in sigma coordinates and written in flux form, include the zonal and meridional momentum equations, the thermodynamic energy equation, the moisture balance, pressure tendency, vertical velocity, and hydrostatic equations. The physical parameterizations include latent heat release due to large-scale saturation that occurs when the relative humidity exceeds 100%, clouds that occur if and only if the model predicts large-scale saturation or cumulus convection, cumulus convection using the Arakawa (1969, 1972) parameterization as modified by Somerville et al. (1974), longwave radiation using the scheme of Krishnamurthy (1982), which is updated every 5 h, and shortwave radiation (Davies 1982), which is updated every 30 min.

The surface boundary fields are obtained from monthly mean climatology datasets. Orography is obtained using the area-weighted averages computed from Gates and Nelson (1975) 1° terrain heights. The ground wetness is obtained from Mintz and Serafini (1981). The surface albedo comes from Sud and Fennessy (1981).

Discretization of the horizontal derivatives is accomplished using an efficient, energy-conserving, fourth-order-accurate finite-difference approximation

on an unstaggered 4° latitude × 5° longitude grid. In order to prevent nonlinear aliasing, a global filtering of the unresolved short waves is performed every 2 h using a 16th-order Shapiro (1970) filter to reduce the amplitude of the waves shorter than four times the grid spacing. In order to avoid using prohibitively short time steps due to the close spacing of the grid points poleward of 60° latitude, additional filtering is performed by multiplying the amplitude of the Fourier components to be filtered by a zonal wavenumber-dependent damping function, as described by Takacs and Balgovind (1983) and Kalnay et al. (1983). For time differencing, the model provides the option of using either the Matsuno (Euler-backward) or a smoothed leapfrog scheme or a combination of both.

3. Properties of the two time-differencing schemes

a. The Matsuno scheme

For a system of partial differential equations of the form

$$\frac{\partial \mathbf{u}}{\partial t} = F(\mathbf{u}), \tag{1}$$

where $F(\mathbf{u})$ represents the nonlinear space differences, the Matsuno (Euler-backward) scheme consists of two steps:

$$\mathbf{u}_{n+1}^* - \mathbf{u}_n = F(\mathbf{u}_n)\Delta t$$

$$\mathbf{u}_{n+1} - \mathbf{u}_n = F(\mathbf{u}_{n+1}^*)\Delta t, \tag{2}$$

where $\mathbf{u}_{n+1}^*$ is an intermediate value in the calculations. A stability analysis method may now be applied to the following simple pure oscillatory equations

$$\frac{\partial u_m}{\partial t} = -m\omega_m u_m, \quad m = 1, 2, \cdots, N, \tag{3}$$

where ω_m is the frequency of the mth component of the field. Substituting (3) into (2) and omitting the subscript gives

$$u_{n+1} - u_n = -i\omega(u_n - i\omega u_n \Delta t)\Delta t = -i\omega u_n \Delta t$$

$$- \omega^2 u_n \Delta t^2 = \left(\frac{\partial u}{\partial t}\right)\Delta t + \left(\frac{\partial^2 u}{\partial t^2}\right)\Delta t^2. \tag{4}$$

Comparing this expression with the Taylor expansion of u near $u^{(n)}$ in time:

$$u_{n+1} - u_n = \left(\frac{\partial u}{\partial t}\right)\Delta t + \frac{1}{2}\left(\frac{\partial^2 u}{\partial t^2}\right)\Delta t^2 + O(\Delta t^3), \tag{5}$$

we note that the Matsuno scheme has introduced a term of $\frac{1}{2}(\partial^2 u/\partial t^2)\Delta t^2$, which acts like a diffusion term in time, to a first-order approximation. If we carry out the standard stability analysis, we will find in the following that the damping effect is wave selective (i.e., wavenumber dependent).

Instead of using (2) we deal with the following simple advective equation

$$\frac{\partial u}{\partial t} = -C\frac{\partial u}{\partial x}. \tag{6}$$

Using a centered differencing scheme for the x derivative and the Matsuno scheme for the time derivative, we obtain

$$u_{m,n+1} = \lambda u_{m,n}$$

$$\lambda = 1 - i\sigma - \sigma^2, \tag{7}$$

where

$$\sigma = \frac{C\Delta t}{\Delta x}\sin k\Delta x. \tag{8}$$

It is evident that the scheme will be damping (also stable) if

$$|\lambda| = (1 - \sigma^2 + \sigma^4)^{1/2} < 1, \tag{9}$$

which holds provided $|\sigma| < 1$.

The first derivative of the amplification factor λ with respect to σ is

$$\frac{\partial|\lambda|}{\partial\sigma} = \frac{2\sigma(2\sigma^2 - 1)}{2(1 - \sigma^2 + \sigma^4)^{1/2}}. \tag{10}$$

This gives

$$\frac{\partial|\lambda|}{\partial\sigma} \begin{cases} <0, & \text{if } 0 < \sigma < \frac{1}{\sqrt{2}}; \\[2mm] =0, & \text{if } \sigma = \frac{1}{\sqrt{2}}; \\[2mm] >0, & \text{if } \frac{1}{\sqrt{2}} < \sigma < 1. \end{cases}$$

Therefore, the strongest damping for the Matsuno scheme occurs when $\sigma = 1/\sqrt{2} = 0.707$.

To insure stability for all wavenumber k requires

$$|C\Delta t/\Delta x| \leqslant 1. \tag{11}$$

This condition is used to determine the time step. Therefore, $\sigma \leqslant 1$ is always true for a numerical model; that is, in the Matsuno scheme the solutions are damped except when $\sigma = 1$. However, the damping is wavenumber dependent, since σ depends on k. For a fixed $C\Delta t/\Delta x$, there is no damping for waves with wavelength $L = 2\Delta x$ ($\sigma = 0$), and damping diminishes when the wavelength L increases (σ decreases). Maximum damping takes place with the combination (L, $C\Delta t/\Delta x$) = ($4\Delta x$, 0.707) or with other pairs of L and $C\Delta t/\Delta x$ that will result in $\sigma = 0.707$. If C represents the wave speed and C_g is the speed of the fastest gravity wave, Δt and Δx are usually chosen so that $C_g\Delta t/\Delta x < 1$. Then, for the slower meteorological waves, one

obtains $C_m\Delta t/\Delta x \ll 1$, which means that slower meteorological waves experience little damping.

In order to better clarify this issue, we will now discuss damping of the Matsuno scheme in terms of the model-assigned values for Δt and Δx and typical values for C (the Rossby waves). Figure 1 presents the amplification factor of the Rossby waves in terms of their nondimensional wavenumbers k for the selectively damping Matsuno scheme. As is evident from this figure, only high wavenumbers of the Rossby waves are slightly affected in their amplifications.

The damping characteristics of the Matsuno scheme may be seen from another viewpoint by writing $C = \omega/k$, where ω is the frequency, from which follows that

$$\sigma = \omega\Delta t\frac{\sin k\Delta x}{k\Delta x}. \tag{12}$$

Since $\sin k\Delta x/k\Delta x < 1$, very low-frequency waves, such as meteorological waves, give a small σ and experience less damping. However, high-frequency waves (e.g., external gravity waves) are generally strongly damped, except for the frequency where $\sigma = k\Delta t = 1$, which is undamped. Internal gravity waves may have low frequencies comparable to meteorological waves and would not be damped much either. As shown by Okland (1972), the Matsuno scheme is not effective for the higher internal modes and also for waves of large horizontal extent or gravity waves in the tropics. Thus, the damping characteristics of the Matsuno time-differencing scheme are rather complex.

As far as the phase-error characteristics are concerned, one can express the amplification factor as

$$\lambda = |\lambda|e^{i\theta}$$

$$\theta = \arctan\frac{\lambda_i}{\lambda_r}, \tag{13}$$

where λ_r and λ_i represent the real and imaginary parts of the complex variable λ. For the Matsuno scheme
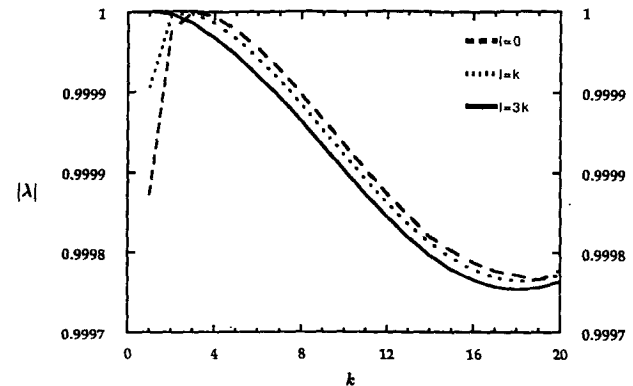

FIG. 1. Amplification factor as a function of Rossby nondimensional wavenumber using the Matsuno scheme.

[see (7)], the relative phase change (see Kurihara 1965) is then given by

$$\frac{\theta}{\sigma} = \frac{1}{\sigma} \arctan \frac{\sigma}{1 - \sigma^2}. \qquad (14)$$

Since σ must be less than unity to ensure stability and rather small for frequencies for which we wish the time-integration-scheme errors to be small, we need to consider (14) for small σ. We then can take only two terms in the Taylor expansion, yielding

$$\frac{\theta}{\sigma} = 1 + \frac{2}{3} \sigma^2 + \cdots \qquad (15)$$

The Matsuno scheme is therefore accelerating.

To provide further insight into the properties of the Matsuno scheme, we present in Fig. 2 the amplification factor and the phase error for the Matsuno scheme as a function of $\Omega = \omega \Delta t$ against the true solution of the advection equation. This confirms that maximum damping occurs at $\Omega = \omega \Delta t = 0.707$ in so far as the amplitude is concerned. The phase acceleration of the Matsuno scheme is evident from Fig. 2b. This phase error increases both with frequency and with the time step. In Fig. 3 the evolution of energy normalized by its initial value is presented for a linearized barotropic primitive equation model using the Matsuno scheme (see Tatsumi 1984). We observe that medium-scale gravity waves (600 km) are totally suppressed during the 2-day integration, while very long gravity waves (4200 km) are only slightly damped during the same integration period.

b. The leapfrog scheme with time smoothing

To discuss the properties of the leapfrog scheme, we use the same advection equation as (6). The leapfrog scheme then assumes the form

$$\frac{u_{m,1} - u_{m,0}}{\Delta t} + C \frac{u_{m+1,0} - u_{m-1,0}}{2\Delta x} = 0$$

$$\frac{u_{m,n+1} - u_{m,n-1}}{2\Delta t} + C \frac{u_{m+1,n} - u_{m-1,n}}{2\Delta x} = 0. \qquad (16)$$

Assuming

$$u_{m,n} = A \exp(n\Delta t) \exp(ikm\Delta x) \qquad (17)$$

and substituting (17) into (16) gives the following complete solution (see details in Haltiner and Williams 1980):

$$u_{m,n} = A \frac{1 + \cos\alpha}{2\cos\alpha} \exp[ik(j\Delta x - n\alpha/k)] + (-1)^{n+1}$$

$$\times A \frac{1 - \cos\alpha}{2\cos\alpha} \exp[ik(j\Delta x + n\alpha/k)], \qquad (18)$$

where $\alpha = \arcsin\sigma$, $\sigma = (C\Delta t/\Delta x) \sin k\Delta x$. If we take the limit $\Delta x \to 0$, $\sigma \to Ck\Delta t$, and then for small Δt, $\alpha = Ck\Delta t$. Now letting $\Delta t \to 0$,

$$A \frac{1 + \cos\alpha}{2\cos\alpha} \exp[ik(j\Delta x - n\alpha/k)] \to$$

$$A \exp[ik(x - Ct)] \qquad (19)$$

which is the true solution of (6), and

$$(-1)^{n+1} A \frac{1 - \cos\alpha}{2\cos\alpha} \exp[ik(i\Delta x + n\alpha/k)] \to 0. \qquad (20)$$

Therefore, the second mode in (18) is a spurious mode that arises from using a second-order difference equation to approximate a first-order differential equation and is a source of error. Note that the second mode, which is referred to as the computational mode, changes sign at every time step due to the factor $(-1)^{n+1}$ and has, thus, essentially a $2\Delta t$ period.
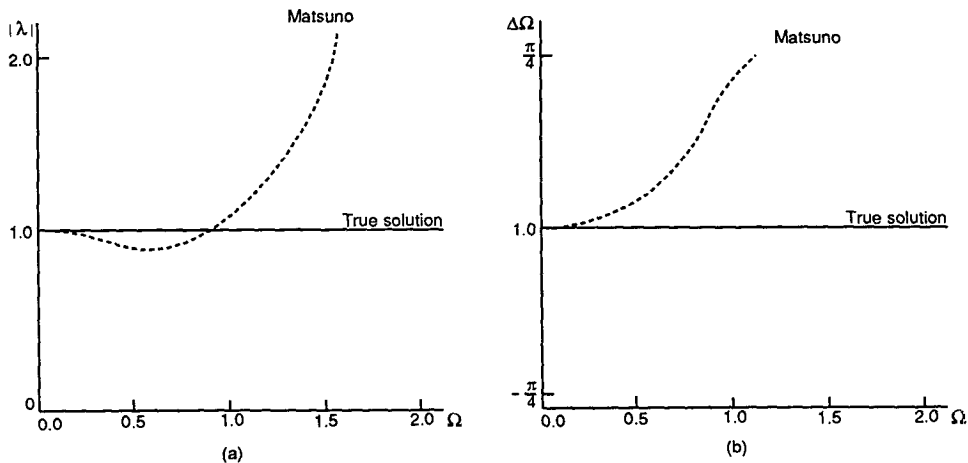

FIG. 2. Amplification factor and the phase error for the Matsuno scheme (dashed line) as a function of $\Omega = \omega \Delta t$ against the true solution (solid line) of the advection equation.
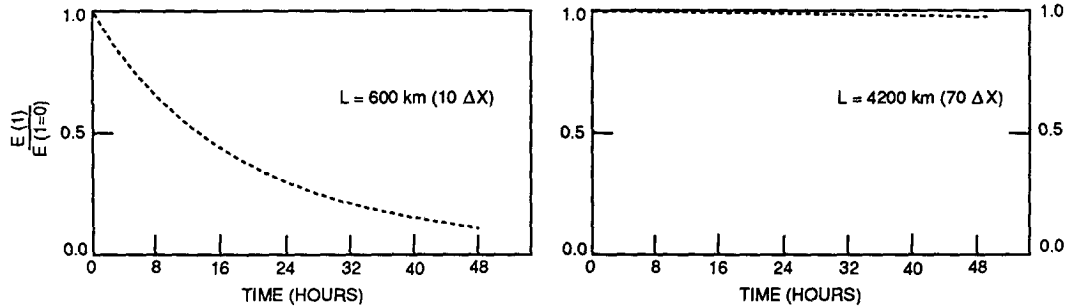
FIG. 3. Evolution of the energy E normalized by its initial value with time using the Matsuno scheme.

An Asselin (1972) filter can be used to remove this computational mode. The filter has no influence on the phase of u [it affects the stability analysis; however, see Haltiner and Williams (1980)].

If one combines the leapfrog time-differencing scheme with the Asselin (1972) filter in the following way

$$u_{m,n+1} = \bar{u}_{m,n-1} + \frac{\Delta t}{\Delta x} (u_{m+1,n} - u_{m-1,n})$$

$$\bar{u}_{m,n} = u_{m,n} + \frac{1}{4} (u_{m,n+1} - 2u_{m,n} + \bar{u}_{m,n-1}), \quad (21)$$

one obtains the so-called smoothed leapfrog scheme in which the computational mode associated with this scheme would appear, in principle, to be removed. In practice, the "odd–even" separation of solutions is still present and must be removed in some way. Kalnay et al. (1983) and Takacs (1986) used one Matsuno time step after every eight leapfrog time steps. In the present application, one Matsuno time step was employed to start the integration, and one was employed after every 11 leapfrog steps. This kept the integration stable for the entire period considered in the present paper, although it eventually became unstable after three months.

Considering the phase error introduced by the leapfrog scheme and taking into account only its physical mode, for which (Haltiner and Williams 1980)

$$\lambda_1 = (1 - \sigma^2)^{1/2} + i\sigma, \quad (22)$$

one obtains

$$\theta_1 = \arctan \frac{\sigma}{(1 - \sigma^2)^{1/2}}. \quad (23)$$

For accuracy, the physical mode phase θ_1 should be as close as possible to the phase change of the solution σ. For small σ we obtain by Taylor expansion

$$\theta_1 = \sigma + \frac{1}{6} \sigma^2 + \cdots. \quad (24)$$

Therefore, the leapfrog scheme is also accelerating; however, its acceleration is four times less than that of

the Matsuno scheme. Differentiating with respect to σ, we have

$$\frac{d\theta_1}{d\sigma} = \frac{1}{(1 - \sigma^2)^{1/2}}. \quad (25)$$

The phase error increases sharply as σ tends to 1; that is, as $\theta_1/\sigma \rightarrow \pi/2$.

In order to provide insight into the evolution of phase-speed errors of the leapfrog scheme, insofar as gravity–inertia waves are concerned, we display in Fig. 4 the phase error in degrees longitude per day as a function of the wavenumber and the time steps. We observe that the phase errors increase for higher wavenumbers and larger time steps.

A general remark is that the additional phase errors that enter the problem due to space differencing are decelerating. Such errors are dominant unless higher-order space-differencing schemes are used. In the pres-
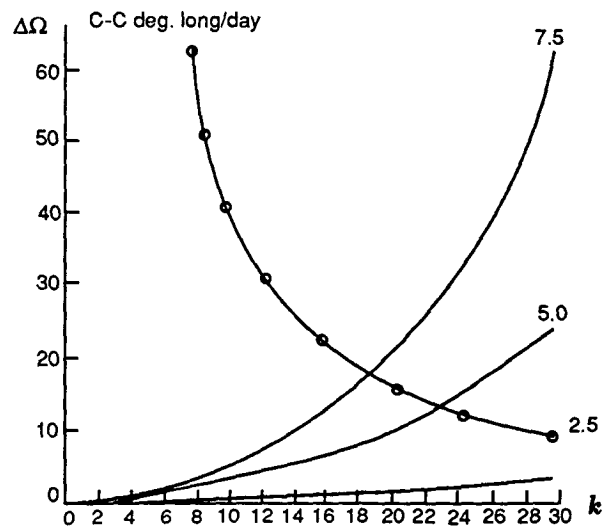
FIG. 4. Phase-speed errors in degrees longitude per day as a function of wavenumber for the gravity–inertia waves using the leapfrog scheme with time steps 2.5, 5.0, and 7.5 min. The curve marked by circles is the wavelength in degrees longitude as a function of wavenumber.

ent case, with the use of a fourth-order spatial discretization, there is no way to tell from a prior analysis whether the deceleration due to the spatial discretization or the acceleration due to the temporal discretization will win in the competition. The analysis does, however, suggest that the synoptic waves in the numerical integration with the Matsuno scheme should travel faster than those in the integration with the leapfrog scheme. This is one of the points we will examine in the following section using an EOF analysis.

4. The numerical experiment and diagnostics

The initial data used for this study were the European Centre for Medium-Range Weather Forecasts' First GARP (Global Atmospheric Research Program) Global Experiment (ECMWF FGGE) IIIb analyses for 0000 UTC 15 December 1978 obtained from the National Center for Atmospheric Research (NCAR). The model was integrated for a 3-month period once with the Matsuno time-differencing scheme and once with the leapfrog scheme with a Matsuno difference every 12th time step. The time steps were each 7.5 min. The data used for the diagnostic study come from the model output for the months of January and February, stored twice per day (at 0000 and 1200 UTC) and interpolated to pressure surfaces. For the purpose of measuring the sensitivity of the seasonal simulation to the method of time differencing, seven different diagnostics are examined. These are (i) the E-P flux and its divergence, (ii) the eddy-induced mean meridional circulation, (iii)

the three-dimensional wave activity flux, (iv) the leading empirical orthogonal functions, (v) the latitudinal distribution of the zonal mean precipitation, (vi) the global distribution of precipitation, and (vii) the kinetic energy spectrum.

The E-P flux divergence,

$$\nabla \cdot \mathbf{F} = \frac{1}{r \cos\phi} \frac{\partial F_\phi \cos\phi}{\partial \phi} + \frac{\partial F_p}{\partial p}, \qquad (26)$$

where

$$F_\phi = \left(-\overline{u'v'} + \frac{\partial \bar{u}}{\partial p} \frac{\overline{v'\theta'}}{\partial \bar{\theta}/\partial p} \right) r \cos\phi$$

$$F_p = \left[\left(f - \frac{\partial \bar{u} \cos\phi}{r \cos\phi \partial\phi} \right) \frac{\overline{v'\theta'}}{\partial \bar{\theta}/\partial p} - \overline{u'\omega'} \right] r \cos\phi,$$

measures the net torque exerted by the eddies on the zonal-mean flow (Eliassen and Palm 1961; Charney and Drazin 1961; Andrews and McIntyre 1976). Here, u and v are the eastward and northward components of the wind velocity, ω is the total rate of change of pressure, θ is potential temperature, p is pressure, f is the Coriolis parameter, ϕ is latitude, r is the radius of the earth, the overbar designates a zonal mean, and the prime represents a departure from this mean. The E-P flux vector $\mathbf{F}$ measures the rate of transfer of wave activity from one location to another in the meridional plane and, for wavelike disturbances, is proportional to the component of the local group velocity in the meridional plane (Edmon et al. 1980). Figure 5 shows
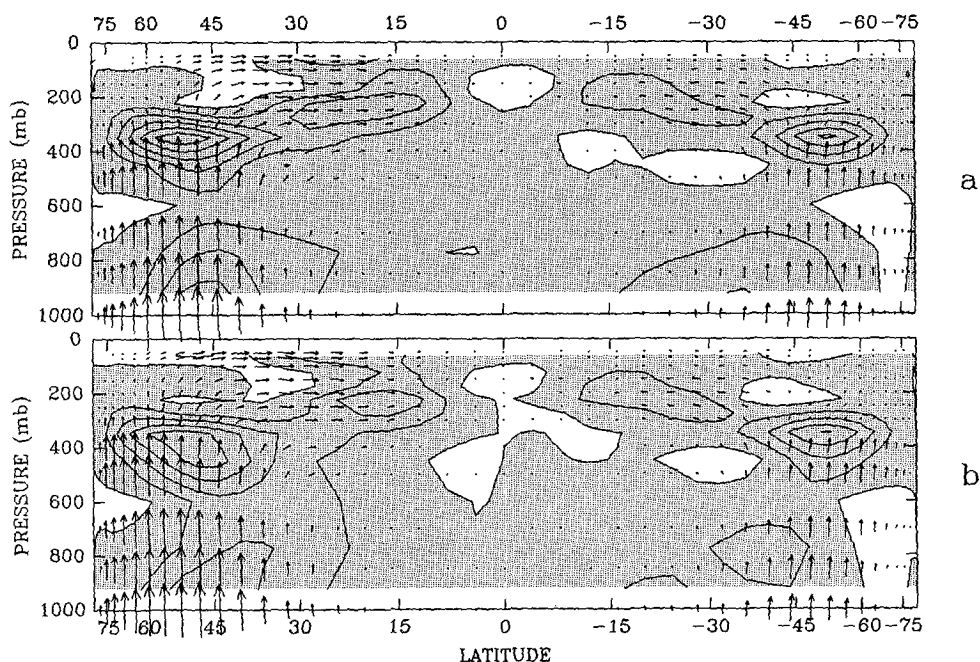

FIG. 5. E-P flux (arrows) and flux divergence (contours) for the period 1 January–28 February 1979, simulated using (a) the leapfrog scheme and (b) the Matsuno scheme. The flux divergences have been divided by the radius of the earth and are contoured in units of 2×10^{-5} m s^{-2}.

the E–P flux (arrows) and flux divergence (contours) for the period 1 January–28 February 1979 using the history tapes from the simulation with (a) the leapfrog scheme and (b) the Matsuno scheme.

The two time-differencing schemes give qualitatively similar pictures of upward E–P flux in the midlatitude troposphere turning equatorward in the upper troposphere and lower stratosphere. Both show flux convergence over most of the troposphere with maxima at midlatitudes, particularly in the winter hemisphere. The primary difference between the two is that the flux convergences are about 20% greater in magnitude with the use of the leapfrog scheme than they are with the use of the Matsuno scheme. In a separate analysis of the contributions of long, medium, and short waves to the E–P flux (not shown here), the same result was found.

Although the primary purpose is to assess the sensitivity of a GCM to time-differencing schemes when the physics package and space discretization are not changed, it is worth noting that the characteristic E–P flux *divergence* in the lower troposphere at mid- and high latitudes (see Edmon et al. 1980) is absent in both numerical integrations. If, as noted by Edmon et al. (1980), this flux divergence is associated with the presence of strong frictional and diabatic boundary-layer processes, the absence of such a divergence in both numerical integrations suggests that the boundary-layer parameterizations in the model are deficient in some respect. In this connection, the NASA Goddard Lab-

oratory for Atmospheres (GLA) has recently revised the parameterization of subgrid-scale processes in its global model using a new second-order closure model for the prediction of turbulent processes (Helfand and Labraga 1988). In the future, it would be of value to repeat the calculations leading to Figs. 5a,b with the new parameterizations to see if the comparison with the FGGE data is improved.

Another useful zonal mean diagnostic is the conventional Eulerian mean meridional circulation induced by the large-scale poleward eddy fluxes of heat and momentum (Eliassen 1952; Kuo 1956). The value of this diagnostic for the study of tropospheric dynamics has been discussed by Pfeffer (1981, 1987) and by Pfeffer and Lu (1989). The equation governing the eddy-induced zonal-mean meridional circulation is

$$\frac{\partial^2}{\partial \eta^2}\left(-\frac{\partial \bar{\theta}}{\partial p}\psi\right) + \frac{\theta r^2}{\alpha \cos^2\phi}\frac{\partial}{\partial p}\left(\hat{f}\hat{f}\frac{\partial\psi}{\partial p}\right)$$
$$+ \frac{\partial}{\partial \eta}\left(\frac{\partial \bar{\theta}}{\partial \eta}\frac{\partial\psi}{\partial p}\right) + \frac{\theta}{\alpha}\frac{\partial}{\partial p}\left(\frac{\alpha}{\theta}\frac{\partial \bar{\theta}}{\partial \eta}\frac{\partial\psi}{\partial \eta}\right)$$
$$= \frac{\partial H}{\partial \eta} + \frac{\theta}{\alpha}\frac{\partial M}{\partial p}, \quad (27)$$

where

$$H \equiv \frac{\partial \overline{\theta'v'}\cos\phi}{\partial \eta} + r\frac{\partial \overline{\theta'\omega'}}{\partial p}$$
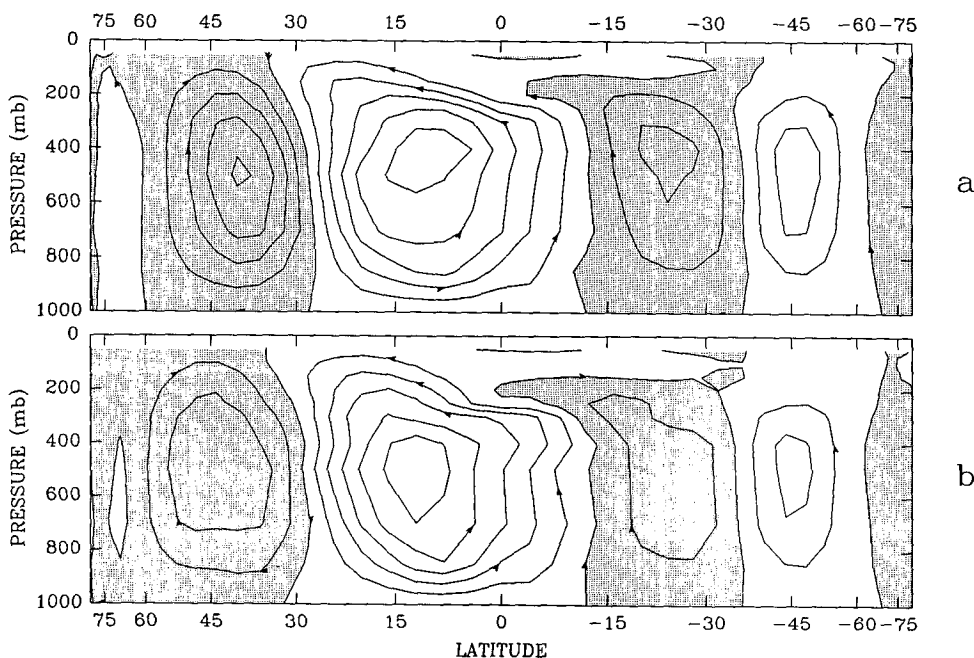

FIG. 6. Eddy-induced streamfunction ψ for the period 1 January–28 February 1979, obtained by solving (39) using the history tapes from the simulation with (a) the leapfrog scheme and (b) the Matsuno scheme. Contour interval 20 m mb s^{-1}.

and

$$M = \frac{r\hat{f}}{\cos^2\phi}\left(\frac{\partial \overline{u'v'}\cos^2\phi}{\partial \eta} + r\cos\phi \frac{\partial \overline{u'\omega'}}{\partial p}\right).$$

Here, $\eta = \sin\phi$, $\hat{f}$ is the absolute vorticity of the zonal-mean current, $\hat{f} \equiv f + 2\bar{u}\tan\phi/r$, α is the specific volume, and ψ is the streamfunction for the zonal-mean meridional circulation in conventional Eulerian diagnostics, defined by

$$\bar{v} = \frac{1}{\cos\phi}\frac{\partial \psi}{\partial p} \quad ; \quad \bar{\omega} = -\frac{1}{r}\frac{\partial \psi}{\partial \eta}. \quad (28)$$

Figure 6 shows the time-mean solutions of (27), subject to the boundary conditions $\psi = 0$ at the poles and at the bottom and top of the atmosphere, obtained using the history tapes from (a) the simulation with the leapfrog scheme and (b) the simulation with the Matsuno scheme. The qualitative features of the two solutions are similar. They show more intense eddy-induced Hadley and Ferrel cells in the Northern (winter) Hemisphere than in the Southern (summer) Hemisphere and weak circulations near the poles. In this respect they resemble the eddy-induced meridional circulations reported by Pfeffer (1981, 1987). As in the case of the E–P fluxes, however, the meridional circulations associated with the Matsuno scheme are somewhat less intense than those associated with the leapfrog scheme.

The three-dimensional counterpart to the E–P flux is the wave activity flux $\mathbf{F}_s$, defined as follows by Plumb (1985):

$$\mathbf{F}_s = p\cos\phi \begin{bmatrix} \left(v'^2 - \frac{1}{2\Omega r\sin2\phi}\frac{\partial v'\Phi'}{\partial \lambda}\right)\mathbf{i} \\ \left(-u'v' + \frac{1}{2\Omega r\sin\phi}\frac{\partial u'\Phi'}{\partial \lambda}\right)\mathbf{j} \\ \frac{2\Omega\sin\phi}{(\partial\hat{T}/\partial z) + (\kappa\hat{T}/H)} \\ \times\left(v'T' - \frac{1}{2\Omega r\sin^2 2\phi}\frac{\partial T'\Phi'}{\partial \lambda}\right)\mathbf{k} \end{bmatrix}, \quad (29)$$

where $\hat{T}$ is the area-averaged temperature on a pressure surface, Φ is the geopotential, Ω is the rate of rotation of the earth, H is a constant scale height, r is the radius of the earth, $\kappa = R/c_p$, the prime represents a departure from the time and zonal mean, and $\mathbf{i}$, $\mathbf{j}$, and $\mathbf{k}$ are unit vectors pointing eastward, northward, and upward, respectively. For diagnostic purposes we will compare the Northern Hemispheric *stationary-wave* activity flux, defined here by letting the prime represent a departure from the zonal mean of the time-averaged field over the 2-month period. Figures 7a and 7b show the stationary-wave activity flux at 500 mb from the simulations with the leapfrog and Matsuno schemes, re-

spectively. The arrows here represent the horizontal flux and the contours the vertical flux. Both fields show major wave trains propagating upward, eastward, and equatorward from eastern Asia into the North Pacific Ocean and eastward across the North Atlantic Ocean. These features resemble, in part, those found by Plumb (1985), although their eastward extent is not as great. There are also secondary centers of upward and downward flux not present in the ten-winter climatological average shown by Plumb. Of interest here, however, are the differences between Figs. 7a and 7b. In particular, the Matsuno scheme gives *larger* three-dimensional stationary-wave activity fluxes and flux divergences than does the leapfrog scheme. Apparently, the damping associated with the Matsuno scheme has less effect on stationary-wave activity than it does on transient-wave activity. It is noted, too, that the secondary maximum of upward and eastward stationary-
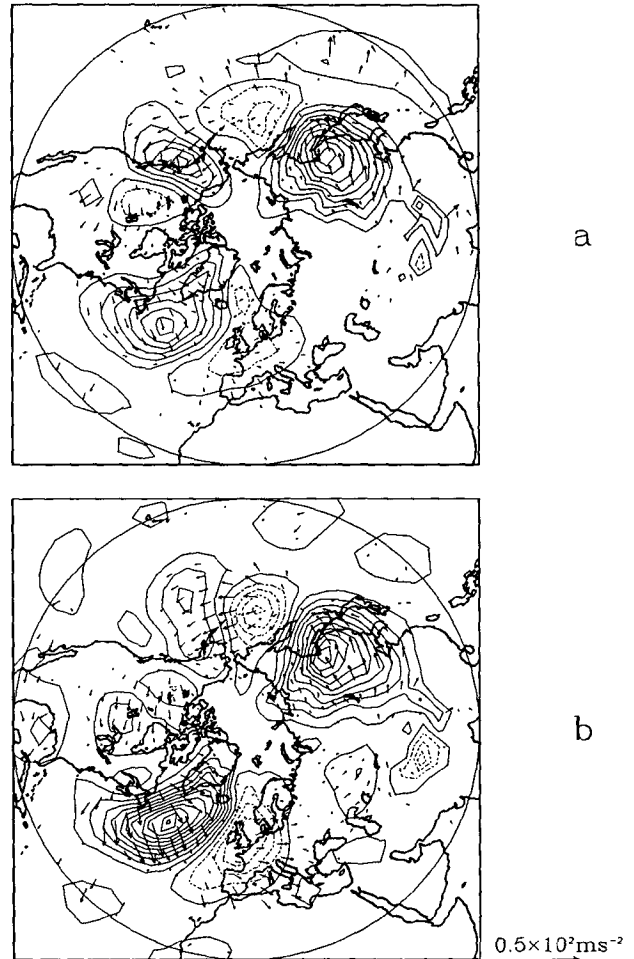

a

b

0.5×10²ms⁻²

Fig. 7. Northern Hemispheric stationary-wave activity flux at 500 mb with (a) the leapfrog scheme and (b) the Matsuno scheme. The magnitude of the arrows representing the horizontal flux is shown in the inset. The contours representing the vertical flux are plotted at values of $(n + \frac{1}{2})\Delta$, where $\Delta = 0.1$ m² s⁻² is the contour interval.

wave activity flux in the eastern Pacific Ocean is found farther to the east in the simulation with the leapfrog scheme than in the one with the Matsuno scheme. Clearly, the climatic differences between the two simulations are not ones that could have been anticipated a priori.

The question of phase errors raised in section 3 is addressed by comparing the two numerical solutions as represented by the sum of the leading complex EOFs and their principal components (PCs). In particular, the variation of the northward component of velocity v at 46°N is analyzed with respect to longitude and time using an empirical orthogonal function expansion of the complex Fourier transform of v, namely,

$$V_n(t) = \sum_{p=1}^{N} A_p(t) C_p(n),$$

in which the condition $\sum_n C_p(n) C_q^*(n) = \delta_{p,q}$ is imposed for orthonormality of the basis functions. The EOFs $C_p(n)$ are determined by a solution of an appropriate eigenvalue problem that maximizes the variance of each successive component (as explained by Pratt and Wallace 1976; Pfeffer et al. 1990) such that more of the variance is compressed into fewer orthogonal functions than in any other representation. The principal components $A_p(t)$ are determined by projecting $V_n(t)$ onto $C_p(n)$. The northward component of velocity is then given by

$$v = \frac{1}{2} \sum_{p=1}^{N} [A_p(t) B_p^*(\lambda) + A_p^*(t) B_p(\lambda)],$$

where λ is longitude and

$$B_p(\lambda) = \sum_{n=1}^{N} C_p^*(n) e^{in\lambda}.$$

For the purpose of comparing the phase propagation characteristics of the waves in the two time-integration schemes, the v field was constructed from a truncated series in which N is the number of EOFs and PCs necessary to account for at least 70% of the variance of this field. In the case of the leapfrog scheme, the first
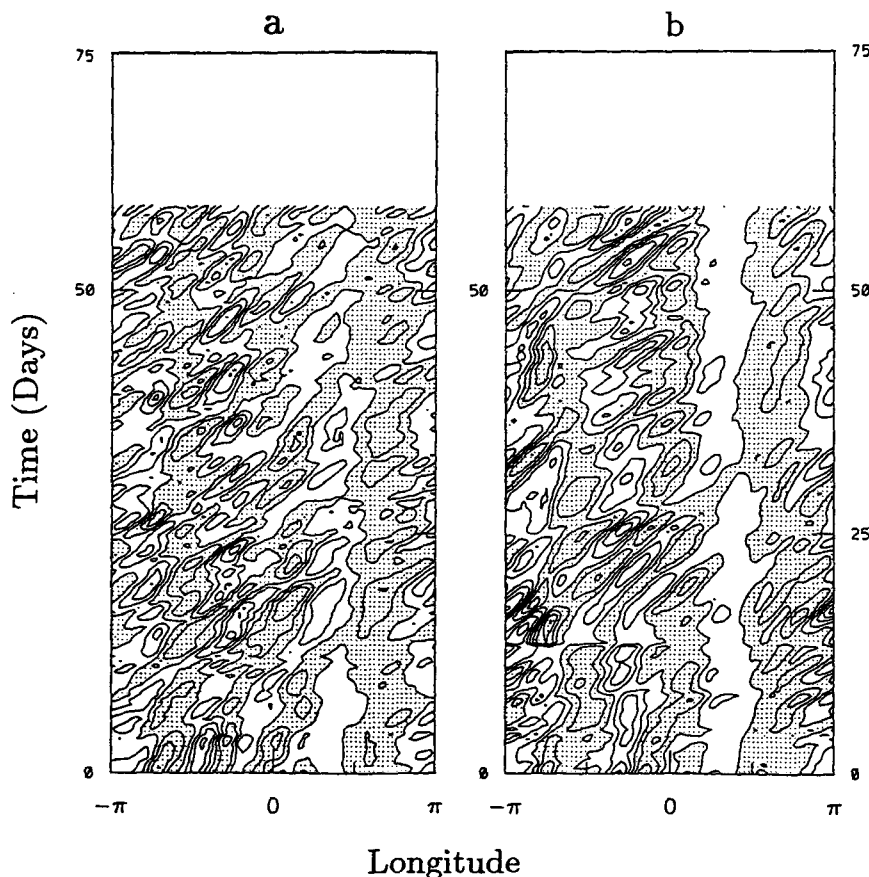

FIG. 8. Contours of v in the λ-t plane constructed by summation of the leading EOFs and PCs. (a) The sum of five EOFs and PCs corresponding to the integration with the leapfrog scheme, accounting for 73.3% of the variance. (b) The sum of four EOFs and PCs corresponding to the integration with the Matsuno scheme, accounting for 71.4% of the variance.

five EOFs accounted for 73.3% of the variance. In the case of the Matsuno scheme, the first four EOFs accounted for 71.4%. Figures 8a and 8b are plots of v constructed from only these leading EOFs as a function of longitude and time for the leapfrog and Matsuno schemes, respectively. The shorter wave scales and higher frequencies appear to be damped in the case of the integration with the Matsuno scheme, as suggested by the linear analysis. It would be difficult, however, to make the case that they travel faster than those obtained with the leapfrog scheme.

We come next to the meridional distributions of zonal-mean precipitation in the simulations with the two time-marching schemes. These are shown in Fig. 9a. The difference between the two curves in this figure (i.e., leapfrog minus Matsuno) is shown in Fig. 9b. In both hemispheres, the extratropical precipitation maximum, which is associated mostly with transient disturbances, is located at a lower latitude in the simulation with the Matsuno scheme than it is in the one with the leapfrog scheme. As a result, the precipitation rate with the leapfrog scheme is about 13% greater at 45°N and about 25% less at 35°N than that with the Matsuno scheme. Significant differences also exist between the two simulations in the latitude belt from 6°S to 6°N. Both precipitation distributions display maxima around 6°N, the greater peak being associated with the use of the Matsuno scheme. As we go south, however, the precipitation rate drops off monotonically in

FIG. 10. Mean precipitation rates for the period 1 January–28 February 1979, simulated with (a) the leapfrog scheme and (b) the Matsuno scheme; (c) the difference between the two (leapfrog minus Matsuno). Contour interval is 2 mm day^{-1}. Shading represents negative values. The data have been smoothed over nine grid points on a 4° latitude × 5° longitude grid.
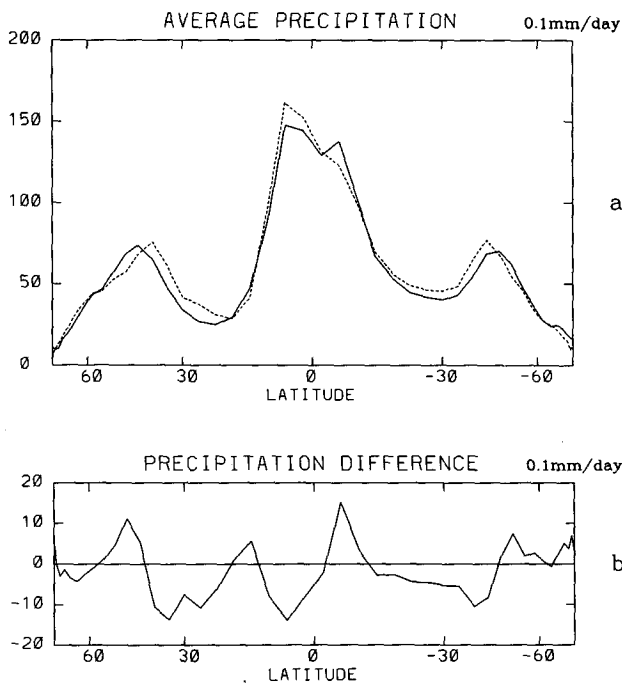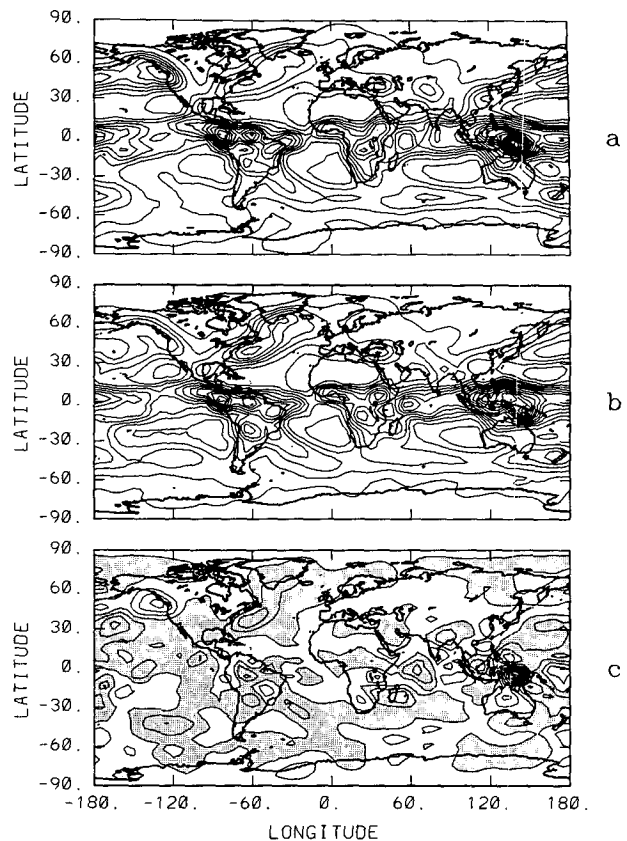
FIG. 9. (a) Zonal-mean precipitation rate for the period 1 January–28 February 1979, simulated with the leapfrog (solid) and Matsuno (dashed) schemes. (b) The difference between the two (leapfrog minus Matsuno).

the simulation with the Matsuno scheme but displays a second peak around 6°S in the one with the leapfrog scheme. As a result, the precipitation rate is almost 10% greater around 6°N and about 10% less around 6°S with the Matsuno scheme than it is with the leapfrog scheme.

We turn now to the geographical distribution of precipitation in the simulations with the two time-marching schemes. Figures 10a and 10b show the distributions simulated with the leapfrog and Matsuno schemes, respectively. Figure 10c shows the difference between the two (namely, leapfrog minus Matsuno). In the Northern Hemispheric midlatitudes the significant difference is the greater precipitation rate associated with the leapfrog scheme in the northeast Pacific Ocean off Canada and the lesser rate in the western North Atlantic off the United States. In the tropics there is an even more striking difference in the precipitation rate in the vicinity of New Guinea, where the leapfrog scheme gives a maximum rate that is about 32% greater than that given by the Matsuno scheme.

Although it is clear that the differences in the tropics

must be due to the greater damping of the shortest eddy scales by the Matsuno scheme, the differences in the midlatitudes cannot easily be explained on the same basis. Current precipitation estimates (for example, from OLR data) are not considered good enough to determine which scheme gives a better simulation, although by most measures the model overestimates the precipitation rate with the use of either scheme.

Figure 11a shows the 2-month mean kinetic energy spectrum for wavenumbers 0–36 in the simulations with the leapfrog (solid) and Matsuno (dashed) schemes. Although waves with wavenumbers less than 9 contain most of the energy, we are interested in the differences at the high-wavenumber end of the spectrum. Accordingly, Fig. 11b presents the portion of the spectrum in the range from wavenumber 9 to 36. In this range the kinetic energy in the simulation with the leapfrog scheme is systematically greater than that in the one with the Matsuno scheme. The weekly mean kinetic energy spectra (not shown here) display the same feature. A breakdown by latitude bands in the tropics and extratropics (not shown here) also displays the same feature. These results are consistent with the damping characteristics of the Matsuno scheme.

5. Conclusions and discussions

We have examined the differences resulting from the use of two time-differencing schemes in simulating the winter mean climate with a GCM—the NASA–
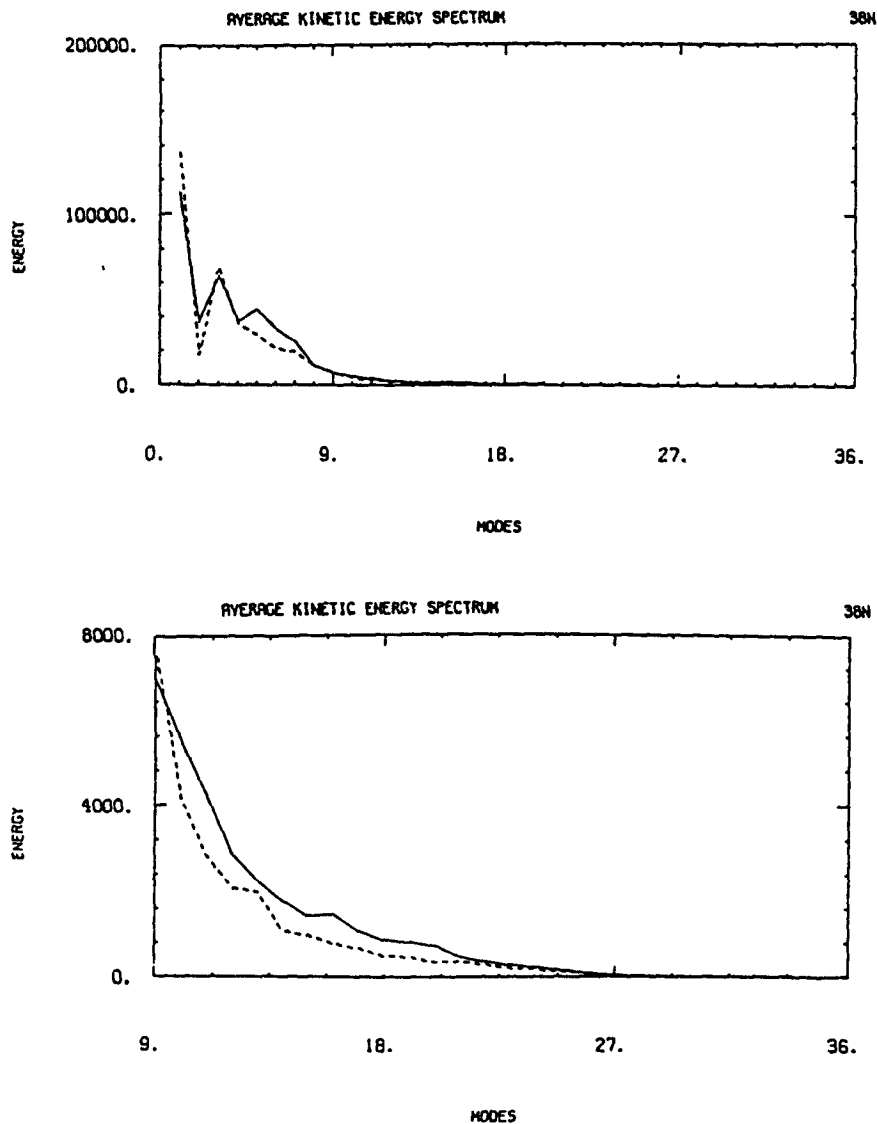

FIG. 11. Kinetic energy spectrum for (a) wavenumber 0–36 and (b) wavenumber 9–36 for the period 1 January–28 February 1979, simulated using the leapfrog scheme (solid) and the Matsuno scheme (dashed).

GLAS fourth-order model—in terms of the E–P flux and its divergence, the eddy-induced mean meridional circulation, the three-dimensional wave activity flux, the leading EOFs, the latitudinal distribution of the zonal mean precipitation, the global distribution of precipitation, and the kinetic energy spectrum. The differences obtained are mostly quantitative. The divergence of the two-dimensional E–P flux and the residual meridional circulation are stronger, and there is more evidence of short-wave activity in the EOF analysis, with the use of the leapfrog scheme than with the use of the Matsuno scheme. The three-dimensional stationary-wave activity flux is greater with the use of the Matsuno scheme. With the leapfrog scheme we obtained a significantly different zonal-mean precipitation distribution than the Matsuno scheme and a much greater local precipitation maximum in the vicinity of New Guinea. The influence of the two time-differencing schemes on the kinetic energy spectrum is such that the Matsuno scheme gives less kinetic energy for wavenumbers greater than 9 due to its selective damping effect.

The main point to be emphasized in this paper is that different methods of discretization, as well as different physical parameterizations, result in significant quantitative differences in climate simulations. We anticipate that this is true not only in the case of time discretizations but also in the case of spatial discretizations. It would be useful, for climate studies, to obtain similar measures of the discrepancies that exist between different spatial discretizations in GCMs with no changes in the physics parameterizations.

REFERENCES

Andrews, D. G., and M. E. McIntyre, 1976: Planetary waves in a horizontal and vertical shear: The generalized Eliassen–Palm relation and the mean zonal acceleration. *J. Atmos. Sci.,* **33,** 2031–2048.

Arakawa, A., 1969: Parameterization of cumulus convection. Proc. *WMO/IUGG Symp. on Numerical Prediction,* Tokyo, 1–6.

——, 1972: Design of the UCLA general circulation model. Numerical Simulation of Weather and Climate. Tech. Rep., No. 7, Department of Meteorology, University of California, Los Angeles, 116 pp.

Asselin, R. A., 1972: Frequency filter for time integrations. *Mon. Wea. Rev.,* **100,** 487–490.

Charney, J. G., 1975: Dynamics of deserts and droughts in the Sahel. *Quart. J. Roy. Meteor. Soc.,* **101,** 193–202.

——, and P. G. Drazin, 1961: Propagation of planetary-scale disturbances from the lower into the upper atmosphere. *J. Geophys. Res.,* **66,** 83–109.

——, and J. Shukla, 1981: Predictability of monsoons. *Monsoon Dynamics,* M. J. Lighthill and R. P. Pearce, Eds., Cambridge University Press, 99–109.

Davies, R., 1982: Documentation of the solar radiation code in the GLAS GCM. NASA Tech. Memo. 83961, 57 pp. [NTIS-N82-30779.]

Edmon, H. J., B. J. Hoskins, and M. E. McIntyre, 1980: Eliassen–Palm cross-sections for the troposphere. *J. Atmos. Sci.,* **37,** 2600–2616.

Eliassen, A., 1952: Slow thermally or frictionally controlled meridional circulation in a circular vortex. *Astrophys. Norv.,* **5,** 19–60.

——, and E. Palm, 1961: On the transfer of energy in stationary mountain waves. *Geofys. Publ.,* **22,** 1–23.

Gates, W. L., and A. B. Nelson, 1975: A new (revised) tabulation of the Scripps topography on a 1° global grid. Part I: Terrain heights. Defense Advanced Research Projects Agency, R-1276-1-ARPA, 132 pp.

Gutowski, W. J., M. J. Iacono, X.-Z. Liang, and W.-C. Wang, 1990: Simulating climate with two different numerical schemes. Tech. Rep. TR049, [DOE/ER-0459T], 56 pp. [Available from Office of Energy Research, Office of Health and Environmental Research, Carbon Dioxide Research Program, Washington, DC 20585.]

Haltiner, G. J., and R. T. Williams, 1980: *Numerical Prediction and Dynamic Meteorology.* 2d ed., John Wiley & Sons, 477 pp.

Helfand, M., and J. C. Labraga, 1988: Design of a nonsingular level 2.5 second-order closure model for the prediction of atmospheric turbulence. *J. Atmos. Sci.,* **45,** 113–132.

Herman, G. F., and W. T. Johnson, 1978: The sensitivity of the general circulation to Arctic sea ice boundaries: A numerical experiment. *Mon. Wea. Rev.,* **106,** 1649–1664.

Kalnay, E., R. Balgovind, W. Chao, D. Edelmann, J. Pfaendtner, L. Takacs, and K. Takano, 1983: Documentation of the GLAS fourth order general circulation model. Volume I: Model documentation. NASA Tech. Memo. 86064, 397 pp. [Available from National Aeronautics and Space Administration, Goddard Space Flight Center, Greenbelt, MD 20771.]

Kasahara, A., 1979: Numerical methods used in atmospheric models. GARP Publication Series No. 17, 449 pp.

Krishnamurthy, V., 1982: The documentation of the Wu-Kaplan radiation parameterization. NASA Tech. Rep. Memo. 83926, 93 pp. [Available from National Aeronautics and Space Administration, Goddard Space Flight Center, Greenbelt, MD 20771.]

Kuo, H. L., 1952: Forced and free meridional circulations in the atmosphere. *J. Meteor.,* **13,** 561–568.

Kurihara, Y., 1965: On the use of implicit and iterative methods for the time integration of the wave equation. *Mon. Wea. Rev.,* **93,** 33–46.

Mesinger, M., and A. Arakawa, 1976: Numerical methods used in atmospheric models. GARP Publication Series No. 17.

Mintz, J., and Y. Serafini, 1981: Monthly normal global fields of soil moisture and land surface evaporation. *Int. Symp. on Variation in Global Water Budget,* Oxford, England.

Okland, H., 1972: On the balance, initialization and data assimilation in primitive equation models. *J. Atmos. Sci.,* **29,** 641–648.

Pfeffer, R. L., 1981: Wave-mean flow interactions in the atmosphere. *Quart. J. Roy. Meteor. Soc.,* **113,** 137–254.

——, 1987: Comparison of conventional and transformed Eulerian diagnostics in the troposphere. *Quart. J. Roy. Meteor. Soc.,* **113,** 237–254.

——, and H. I. Lu, 1989: *An Atlas of FGGE Diagnostics.* Florida State University Publications, 305 pp. [Available from the Geophysical Fluid Dynamical Institute, Florida State University, Tallahassee, FL 32306.]

——, J. Ahlquist, R. Kung, Y. Chang, and G. Li, 1990: A study of baroclinic wave behavior over bottom topography using complex principal component analysis of experimental data. *J. Atmos. Sci.,* **47,** 67–81.

Plumb, R. A., 1985: On the three dimensional propagation of stationary waves. *J. Atmos. Sci.,* **42,** 217–229.

Pratt, R. W., and J. M. Wallace, 1976: Zonal propagation characteristics of large-scale fluctuations in the mid-latitude troposphere. *J. Atmos. Sci.,* **33,** 1184–1194.

Shapiro, R., 1970: Smoothing, filtering, and boundary effects. *Rev. Geophys. Space Phys.,* **8,** 359–387.

Shukla, J., D. Straus, D. Randall, Y. Sud, and L. Marx, 1981: Winter and summer simulations with the GLAS climate model. NASA Tech. Memo. 83866, 282 pp. [Available from Goddard Space Flight Center, Greenbelt, MD 20771.]

Simmons, A. J., and L. Bengtsson, 1984: *The Global Climate.* Cambridge University Press, 233 pp.

Somerville, R. C. J., P. H. Stone, M. Halem, J. E. Hansen, J. S. Hogan, L. M. Druyan, G. Russell, A. A. Lacis, W. J. Quirk, and J. Tenenbaum, 1974: The GISS model of the global atmosphere. *J. Atmos. Sci.,* **31,** 84–117.

Sud, Y. C., and M. Fennessy, 1981: A study of the influence of surface albedo on July circulation in semi-arid regions using the GLAS GCM. *J. Climatol.,* **2,** 105–125.

Takacs, L. L., 1986: Documentation of the Goddard laboratory for atmospheres fourth order two-layer shallow water model. NASA Tech. Memo., 86227, 84 pp. [Available from National Aeronautics and Space Administration, Goddard Space Flight Center, Greenbelt, MD 20771.]

——, and R. Balgovind, 1983: High latitude filtering in global gridpoint models. *Mon. Wea. Rev.,* **111,** 2005–2015.

Tatsumi, Y., 1984: Time integration methods used in atmospheric models. *Workshop on Limited-Area Numerical Weather Prediction Models for Computers of Limited-Power. Part II.* Erice, Italy, WMO, 43–105.

Wallace, J. M., S. Tibaldi, and A. J. Simmons, 1983: Reduction of systematic forecast errors in the ECMWF model through introduction of an envelope topography. *Quart. J. Roy. Meteor. Soc.,* **109,** 683–717.